Mechanics of Materials 64 (2013) 135–141

Contents lists available at SciVerse ScienceDirect

Mechanics of Materials

journal homepage: www.elsevier.com/locate/mechmat

A first-principles study of the mechanical properties of g-GeC

Qing Peng *, Chao Liang, Wei Ji, Suvranu De

Department of Mechanical, Aerospace and Nuclear Engineering, Rensselaer Polytechnic Institute, Troy, NY 12180, USA

ARTICLE INFO

Article history:
Received 22 October 2012
Received in revised form 22 February 2013
Available online 29 May 2013

Keywords:
Mechanical properties
High order elastic constants
Density functional theory
2D materials
Honeycomb structure
g-GeC

ABSTRACT

We investigate the mechanical properties of graphene-like hexagonal germanium carbide monolayers (*g*-GeC) using first-principles calculations based on density-functional theory. Compared to graphene, *g*-GeC is much softer, with 41% in-plane stiffness, 44%, 42% and 37% ultimate strengths in *armchair*, *zigzag*, and *biaxial* strains respectively, as well as smaller ultimate strains. However, *g*-GeC has a larger Poisson's ratio, 0.28, about 1.5 times that of graphene. We obtained the second, third, fourth, and fifth order elastic constants for a rigorous continuum description of the elastic response of *g*-GeC. The second order elastic constants, including in-plane stiffness, are predicted to monotonically increase with pressure while the Poisson's ratio monotonically decreases with increasing pressure. The sound velocity of a compressional wave has a minima at an in-plane pressure of −7 GPa while that of a shear wave monotonically with pressure.

1. Introduction

Hexagonal germanium carbide monolayer (*g*-GeC) is a graphene-like 2D material which has attracted considerable interest due to its promising applications in optoelectronics and energy engineering (Şahin et al., 2009; Chigo Anota and Murrieta Hernandez, 2011; Lu et al., 2012). With a predicted wide band gap (> 3 eV), *g*-GeC is a good candidate for fabrication of blue and ultraviolet light emitting diodes, as well as photovoltaic applications (Shim et al., 1998; Sari et al., 2003; Ueno et al., 2006; Brazier and Ruiz, 2011; Mahmood and Sansores, 2005; Ganguly et al., 1991). It is also applicable for design and preparation of multilayer anti-reflection and protection coatings of infrared (IR) windows. Very recently, it was predicted that the indirect-direct band gap transition of *g*-GeC can be tuned by strain engineering (Lu et al., 2012). However, it is unclear that *g*-GeC can sustain such engineering since large strains were blindly applied without considering its mechanical instabilities. Without knowledge of the mechanical properties, this engineered strain might not be physical. Thus a systematic study of the mechanical properties including nonlinear elastic behaviors at large strains are highly desired. In spite of its importance, the mechanical properties are not studied to our best knowledge.

Several previous studies have shown that 2D monolayers present a large nonlinear elastic deformation during the tensile strain up to the ultimate strength of the material, followed by a strain softening until fracture (Lee et al., 2008; Liu et al., 2007; Xiao et al., 2004; Khare et al., 2007; Lu and Huang, 2009; Peng et al., 2012a; Peng et al., 2012b; Peng et al., 2012c). We expect that the *g*-GeC behaves in a similar manner. Under large deformation, the strain energy density needs to be expanded as a function of strain in a Taylor series to include quadratic and higher order terms (Hiki, 1981; Cadelano et al., 2009). The higher order terms account for both nonlinearity and strain softening of the elastic deformation. They can also express other anharmonic properties of 2D nanostructures including phenomena such as thermal expansion, phonon–phonon interaction, etc. (Lee et al., 2008).

The goal of this paper is to study the mechanical behaviors of *g*-GeC at large strains and find an accurate continuum description of the elastic properties from *ab initio* density functional theory calculations. The total energies of the system, forces on each atoms, and stresses on the

* Corresponding author. Tel.: +1 518 279 6669; fax: +1 518 276 6025.
E-mail address: qpeng.org@gmail.com (Q. Peng).
URL: http://qpeng.org (Q. Peng).

0167-6636/$ - see front matter © 2013 Elsevier Ltd. All rights reserved.
http://dx.doi.org/10.1016/j.mechmat.2013.05.009

simulation boxes are directly obtained from DFT calculations. The response of *g*-GeC under the nonlinear deformation and fracture are studied, including ultimate strength and ultimate strain. The high order elastic constants are obtained by fitting the stress–strain curves to analytical stress–strain relationships that belong to the continuum formulation (Peng et al., 2012a; Wei et al., 2009). We compared this proposed new material with the well known 2D materials such as graphene (Wei et al., 2009), graphyne (Peng et al., 2012c) and *g*-BN (graphene-like hexagonal boron nitride monolayer) (Peng and De, 2012; Peng et al., 2012b, 2013a). Based on our result of the high order elastic constants, the pressure dependence properties, such as sound velocities and the second order elastic constants, including the in-plane stiffness, are predicted. Our results for the continuum formulation could also be useful in finite element modeling of the multiscale calculations for mechanical properties of *g*-GeC at the continuum level. The remainder of the paper is organized as follows. Section 2 presents the computational method, including the computational details of DFT calculations and the basic nonlinear elastic theory applied to 2D hexagonal structures. The results and analysis are in Section 3, followed by conclusions in Section 4.

2. Density functional theory calculations

We consider a conventional unit cell containing 6 atoms (3 carbon atoms and 3 germanium atoms) with periodic boundary conditions (Fig. 1). The 6-atom conventional unit cell is chosen because there is a soft mode leading to mechanical instability, and this key factor in limiting the strength of monolayer materials can only be captured in unit cells with hexagonal rings (Marianetti and Yevick, 2010).

The total energies of the system, forces on each atoms, stresses, and stress–strain relationships of *g*-GeC under the desired deformation configurations are characterized via first-principles calculations with density-functional theory (DFT). DFT calculations were carried out with the Vienna Ab-initio simulation package (VASP) (Kresse and Hafner, 1993, 1994; Kresse and Furthuller, 1996a; Kresse and Furthuller, 1996b) which is based on the Kohn–Sham density functional theory (KS-DFT) (Hohenberg and Kohn, 1964; Kohn and Sham, 1965) with the generalized gradient approximations as parameterized by Perdew, Burke and Ernzerhof (PBE) for exchange–correlation functions (Perdew et al., 1996). The electrons explicitly included in the calculations are the ($2s^2 2p^2$) electrons. The core electrons ($1s^2$) are replaced by the projector augmented wave (PAW) and pseudo-potential approach (Blöchl, 1994; Jones and Gunnarsson, 1989). A plane-wave cutoff of 600 eV is used in all the calculations. The calculations are performed at zero temperature.

The criterion to stop the relaxation of the electronic degrees of freedom is set by total energy change to be smaller than 0.000001 eV. The optimized atomic geometry was achieved through minimizing Hellmann–Feynman forces acting on each atom until the maximum forces on the ions were smaller than 0.001 eV/Å.

The atomic structures of all the deformed and undeformed configurations are obtained by fully relaxing a 6-atom-unit cell where all atoms were placed in one plane. The simulation invokes periodic boundary conditions for the two in-plane directions while the displacement to out-of-plane direction is forbidden.

The irreducible Brillouin zone was sampled with a gamma-centered $17 \times 17 \times 1$ *k*-mesh. Such a large *k*-mesh was used to reduce the numerical errors caused by the strain of the systems. The initial charge densities were taken as a superposition of atomic charge densities. There was a 15 Å thick vacuum region to reduce the inter-layer interaction to model the single layer system. To eliminate the artificial effect of the out-of-plane thickness of the simulation box on the stress, we used the second Piola–Kirchhoff (P-K) stress (Peng et al., 2012a) to express the 2D forces per length with units of N/m.

For a general deformation state, the number of independent components of the second, third, fourth, and fifth order elastic tensors are 21, 56, 126, and 252 respectively (Hiki, 1981). However, there are only fourteen independent elastic constants need to be explicitly considered due to the symmetries of the atomic lattice point group D_{6h} which consists of a sixfold rotational axis and six mirror planes (Wei et al., 2009).

The fourteen independent elastic constants of *g*-GeC are determined by a least-squares fit to the stress–strain results from DFT based first-principles studies in two steps, detailed in our previous work (Peng et al., 2012a), which had been well used to explore the mechanical properties of 2D materials (Peng et al., 2012d; Peng et al., 2013b; Peng et al., 2013c; Peng et al., 2013d; Peng et al., 2013e). A brief introduction is that, in the first step, we use a least-squares fit to five stress–strain responses. Five relationships

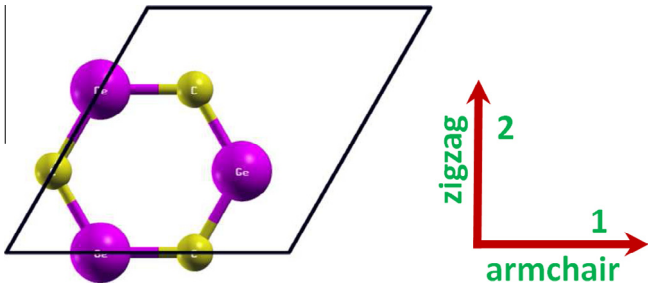

Fig. 1. Atomic structure of *g*-GeC in the conventional unit cell (6 atoms) in the undeformed reference configuration.

between stress and strain are necessary because there are five independent fifth-order elastic constants (FFOEC). We obtain the stress–strain relationships by simulating the following deformation states: uni-axial strain in the zigzag direction (*zigzag*); uni-axial strain in the armchair direction (*armchair*); and equibiaxial strain (*biaxial*). From the first step, the components of the second-order elastic constants (SOEC), the third-order elastic constants (TOEC), and the forth-order elastic constants (FOEC) are over-determined (i.e, the number of linearly independent variables are greater than the number of constrains), and the FFOEC are well-determined (the number of linearly independent variables are equal to the number of constrains). Under such circumstances, the second step is needed: least-square solution to these over- and well-determined linear equations.

3. Results and analysis

3.1. Atomic structure

We first optimize the equilibrium lattice constant for *g*-GeC. The total energy as a function of lattice spacing is obtained by specifying seven lattice constants varying from 5.57 Å to 5.63 Å, with full relaxations of all the atoms. A least-square fit of the energies versus lattice constants with a fourth-order polynomial function yields the equilibrium lattice constant as $a = 5.598$ Å. The most energetically favorable structure is set as the strain-free structure in this study and the atomic structure, as well as the conventional cell is shown in Fig. 1. Specifically, the bond length of C–Ge bond is 1.87 Å, which is 0.45 Å (or 32%) longer than that in graphene. The C–Ge–C and Ge–C–Ge angles are 120° and all atoms are within one plane. Our result of *g*-GeC's atomic structure is in good agreement with previous DFT calculations (Şahin et al., 2009; Lu et al., 2012).

3.2. Strain energy

When the strains are applied, all the atoms are allowed full freedom of motion within their plane. A quasi-Newton algorithm is used to relax all atoms into equilibrium positions within the deformed unit cell that yields the minimum total energy for the imposed strain state of the super cell.

Both compression and tension are considered with Lagrangian strains ranging from −0.2 to 0.3 with an increment of 0.01 in each step for all three deformation modes. We define strain energy per atom $E_s = (E_{tot} - E_0)/n$, where E_{tot} is the total energy of the strained system, E_0 is the total energy of the strain-free system, and $n = 6$ is the number of atoms in the unit cell. This size-independent quantity is used for the comparison between different systems. Fig. 2 shows the E_s of *g*-GeC as a function of strain in uniaxial armchair, uniaxial zigzag, and biaxial deformation. E_s is seen to be anisotropic with strain direction. E_s is asymmetric for compression ($\eta < 0$) and tension ($\eta > 0$) for all three modes. This asymmetry indicates the anharmonicity of the *g*-GeC structures.

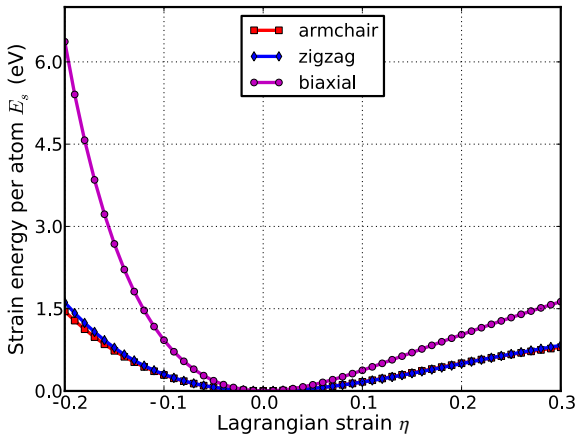

Fig. 2. Energy–strain responses for uniaxial strain in armchair and zigzag directions, and biaxial strains.

The harmonic region where the E_s is a quadratic function of applied strain can be taken between $-0.02 < \eta < 0.02$. The stresses, derivatives of the strain energies, are linearly increasing with the increase of the applied strains in the harmonic region. The anharmonic region is the range of strain where the linear stress–strain relationship is invalid and higher order terms are not negligible. With even larger loading of strains, the systems will undergo irreversible structural changes, and the systems are in plastic region where they may fail. The maximum stain in the anharmonic region is the *critical* strain. For all three directions, the critical strains are not spotted in the testing range. The ultimate strains are determined as the corresponding strain of the ultimate stress, which is the maxima of the stress–strain curve, as discussed in the following section.

It is worth noting that in general the compressive strains will cause rippling of the *free-standing* thin films, membranes, plates, and nanosheets (Cerda and Mahadevan, 2003). The critical compressive strain for rippling instability is much less than the critical tensile strain for fracture, for example, 0.0001% versus 2% in graphene sheets (Zhang and Liu, 2011). However, the rippling can be suppressed by applying constraint, such as embedding (0.7%) (Tsoukleri et al., 2009), substrate (0.4% before heating) (Bao et al., 2009), thermal cycling on SiO_2 substrate (0.05%) (Yoon et al., 2011) and BN substrate (0.6%) (Pan et al., 2012), and sandwiching (Quhe et al., 2012). Our study of compressive strains is important in understanding the mechanics of these non-rippling applications. The rippling phenomena are interesting and important, which is, however, out the scope of this study.

3.3. Stress–strain curves

The second P–K stress versus Lagrangian strain relationship for uniaxial strains along the armchair and zigzag directions, as well as biaxial strains are shown in Fig. 3. The stresses are the derivatives of the strain energies with respect to the strains. The ultimate strength is the maximum stress that a material can withstand while being

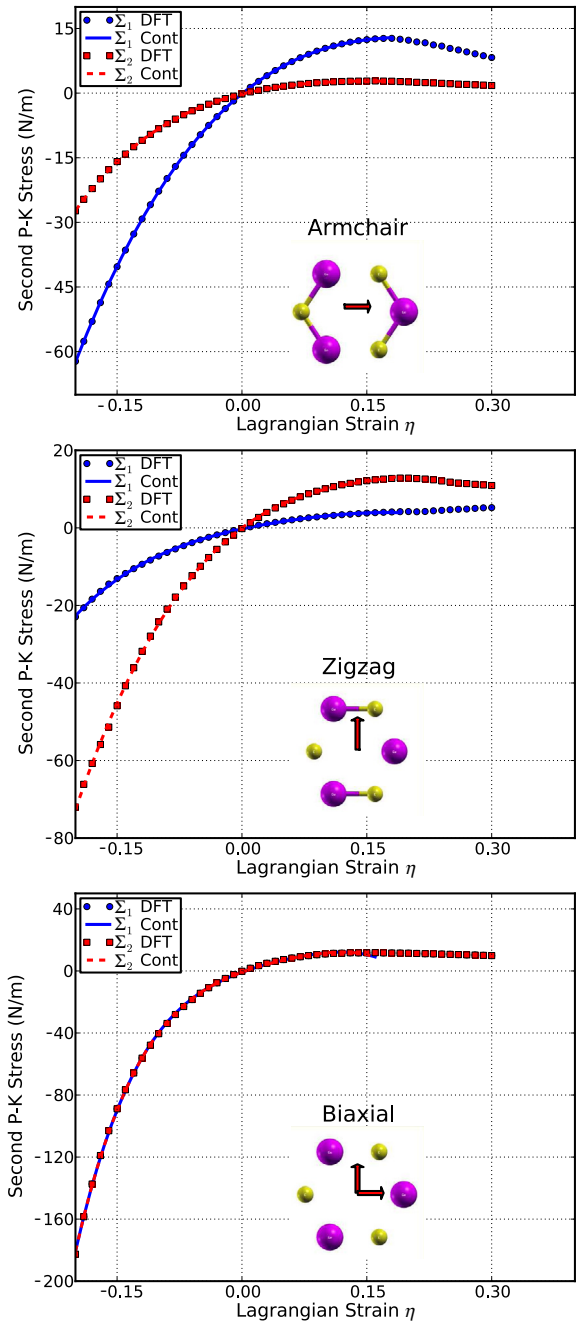

Fig. 3. Stress–strain responses of *g*-GeC under the armchair, zigzag and biaxial strain. Σ_1 (Σ_2) denotes the x (y) component of stress. "Cont" stands for the fitting of DFT calculations ("DFT") to continuum elastic theory.

stretched, and the corresponding strain is the ultimate strain. Under ideal conditions, the critical strain is larger than the ultimate strain. The systems of perfect *g*-GeC under strains beyond the ultimate strains are in a metastable state, which can be easily destroyed by long wavelength perturbations, vacancy defects, as well as high temperature effects (Topsakal et al., 2010). The ultimate strain is determined by the intrinsic bonding strengths and acts as a lower limit of the fraction strain. Thus it has a practical meaning in considering for its applications.

The ultimate strengths and strains corresponding to the different strain conditions are in Table 1, compared with that of graphene (Wei et al., 2009), graphyne (Peng et al., 2012c), and *g*-BN (Peng et al., 2012a). The material behaves in an asymmetric manner with respect to compressive and tensile strains. With increasing strains, the C–Ge bonds are stretched and eventually rupture. When the strain is applied in the armchair direction, the bonds of those parallel with this direction are more severely stretched than those in other directions. The ultimate strain in armchair deformation is 0.18, same as that of *g*-BN, but smaller than graphene (0.19) and graphyne (0.20). Under the zigzag deformation, in which the strain is applied perpendicular to the armchair, there is no bond parallel to this direction. The bonds incline to the zigzag direction with an angle of 30° are more severely stretched than those in the armchair direction. The ultimate strain in this zigzag deformation is 0.19. At this ultimate strain, the bonds that are at an incline to the armchair direction appear to be ruptured (Fig. 3 middle panel). Under the biaxial deformation, the ultimate strain is η_m^b=0.16, where all the C–Ge bonds are observed to be ruptured (Fig. 3 bottom)

It should be noted that the softening beyond the ultimate strains only occurs for ideal conditions. The systems under this circumstance are in a metastable state. Thus only the data within the ultimate strain has physical meaning and was used in determining the high order elastic constants in the following subsection.

which can be easily destroyed by long wavelength perturbations, vacancy defects, as well as high temperature effects, and enter a plastic state (Topsakal et al., 2010).

3.4. Elastic constants

The elastic constants are critical parameters in finite element analysis models for mechanical properties of materials. Our results of these elastic constants provide an accurate continuum description of the elastic properties of *g*-GeC from *ab initio*density functional theory calculations. They are suitable for incorporation into numerical methods such as the finite element technique.

The second order elastic constants model the linear elastic response. The higher (>2) order elastic constants are important to characterize the nonlinear elastic response of *g*-GeC using a continuum description. These can be obtained using a least squares fit of the DFT data and are reported in Table 2. Corresponding values for graphene (Wei et al., 2009), graphyne (Peng et al., 2012c), and *g*-BN (Peng et al., 2012a) are also listed for a rough comparison of *g*-GeC to those known materials.

The in-plane Young's modulus Y_s and Poison's ratio ν may be obtained from the following relationships: $Y_s = (C_{11}^2 - C_{12}^2)/C_{11}$ and $\nu = C_{12}/C_{11}$. Our results of $Y_s = 143.8$ (N/m) and $\nu = 0.281$ agree with a previous *ab initio* study ($Y_s = 142$ (N/m) and $\nu = 0.33$) (Şahin et al., 2009). The in-plane stiffness of *g*-GeC is small compared to graphene. This could be a result of the weakened bond of Ge-C compared to the C-C bond in graphene. From the aspect of bond, the bond length in *g*-GeC is 1.87 Å, about

Table 1
Ultimate strengths (Σ_m^a, Σ_m^z, Σ_m^b) in units of N/m and ultimate strains (η_m^a, η_m^z, η_m^b) under uniaxial strain (armchair and zigzag) and biaxial from DFT calculations, compared with graphene, graphyne and *g*-BN.

	g-GeC	Graphene (Wei et al., 2009)	Graphyne (Peng et al., 2012c)	*g*-BN (Peng et al., 2012a)
Σ_m^a	12.7	29.5	17.8	23.6
η_m^a	0.18	0.19	0.20	0.18
Σ_m^z	12.8	31.4	18.8	26.3
η_m^z	0.19	0.24	0.20	0.26
Σ_m^b	11.8	33.1	20.64	27.8
η_m^b	0.16	0.24	0.18	0.24

Table 2
Nonzero independent components for the SOEC, TOEC, FOEC, and FFOEC tensor components, in-plane stiffness Y_s (units of N/m), and Poisson's ratio v of *g*-GeC from DFT calculations, compared with graphene, graphyne and *g*-BN.

	g-GeC	Graphene (Wei et al., 2009)	Graphyne (Peng et al., 2012c)	*g*-BN (Peng et al., 2012a)
a (Å)	3.232	2.446	6.889	2.512
Y_s	143.8	348	162.1	278.3
v	0.281	0.169	0.429	0.218
C_{11}	156.1	358.1	198.7	293.2
C_{12}	43.9	60.4	85.3	66.1
C_{111}	−1412.7	−2817	−890.9	−2513.6
C_{112}	−155.3	−337.1	−872.6	−425.0
C_{222}	−1186.2	−2693.3	−1264.2	−2284.2
C_{1111}	8207	13416.2	−7966	16547
C_{1112}	2495	759	4395	2609
C_{1122}	5770	2582.8	8662	2215
C_{2222}	4777	10358.9	1154	12288
C_{11111}	638	−31383.8	89000	−65265
C_{11112}	−43162	−88.4	−10393	−8454
C_{11122}	−50243	−12960.5	−26725	−28556
C_{12222}	−30954	−13046.6	−15495	−26955
C_{22222}	−4247	−33446.7	−14262	−100469

32 percents larger than that of graphene (1.42 Å). The bonds can be viewed as being stretched in prior by the introducing of germanium atoms, in reference to pristine graphene. These stretched bonds are weaker than those un-stretched, resulting a reduction of the mechanical strength.

Knowledge of higher order elastic constants is very useful in understanding the anharmonicity. Specially, the third order elastic constants are important in understanding the nonlinear elasticity of materials such as changes in acoustic velocities due to finite-strain.

Stress–strain curves in the previous section show that they will soften when the strain is larger than the ultimate strain. From the view of electron bonding, this is due to the bond weakening and breaking. This softening behavior is determined by the TOECs and FFOECs in the continuum aspect. The negative values of TOECs and FFOECs ensure the softening of *g*-GeC monolayer under large strain.

The hydrostatic terms ($C_{11}, C_{22}, C_{111}, C_{222}$, and so on) of *g*-GeC monolayers are smaller than those of graphene and *g*-BN, consistent with the conclusion that the *g*-GeC is "softer". The shear terms ($C_{12}, C_{112}, C_{1122}$, etc.) in general are larger than those of graphene, which contributes to its lower compressibility. Compared to graphene, graphyne, and *g*-BN, one can conclude that the mechanical behavior of *g*-GeC is similar to graphyne, and much softer than graphene and *g*-BN.

3.5. Pressure effect on the elastic moduli

With third-order elastic moduli, we can study the effect of the second-order elastic moduli on the pressure p acting in the plane of *g*-GeC. Explicitly, when pressure is applied, the pressure dependent second-order elastic moduli ($\tilde{C_{11}}, \tilde{C_{12}}, \tilde{C_{22}}$) can be obtained from C_{11}, C_{12}, C_{22}, C_{111}, C_{112}, C_{222}, Y_s, and v as:

$$\tilde{C_{11}} = C_{11} - (C_{111} + C_{112})\frac{1-v}{Y_s}P, \tag{1}$$

$$\tilde{C_{22}} = C_{11} - C_{222}\frac{1-v}{Y_s}P \tag{2}$$

$$\tilde{C_{12}} = C_{12} - C_{112}\frac{1-v}{Y_s}P \tag{3}$$

The second-order elastic moduli of *g*-GeC are seen to increase linearly with the applied pressure (Fig. 4). Poisson's ratio also increases monotonically with the increase of pressure. $\tilde{C_{11}}$ is not symmetrical to $\tilde{C_{22}}$ any more. $\tilde{C_{11}} = \tilde{C_{22}} = C_{11}$ only occurs when the pressure is zero. This anisotropy could be the outcome of anharmonicity.

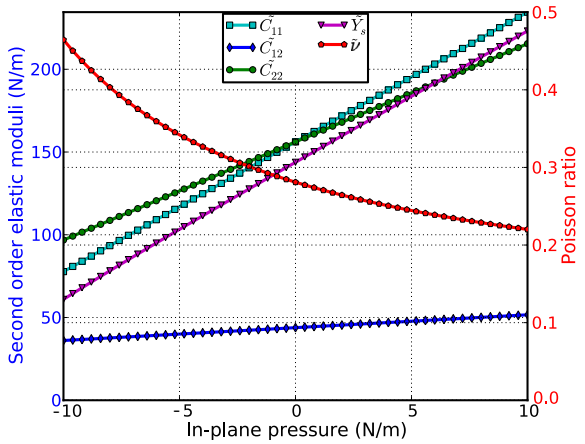

Fig. 4. Second-order elastic moduli and Poisson ratio as function of the pressure.

3.6. Pressure effect on the velocities of sound

In the *g*-GeC monolayer, there are non-zero in-plane Young's moduli and shear deformations. Hence, it is possible to generate sound waves with different velocities depending on the deformation mode. Sound waves generating biaxial deformations (compressions) are compressional or *p*-waves. Sound waves generating shear deformations are shear or *s*-waves. The sound velocities of these two types of waves are calculated from the second-order elastic moduli and mass density using the following relations:

$$v_p = \sqrt{\frac{\tilde{Y}_s(1-\tilde{\nu})}{\rho_m(1+\tilde{\nu})(1-2\tilde{\nu})}}, \tag{4}$$

$$v_s = \sqrt{\frac{\tilde{C}_{12}}{\rho_m}}. \tag{5}$$

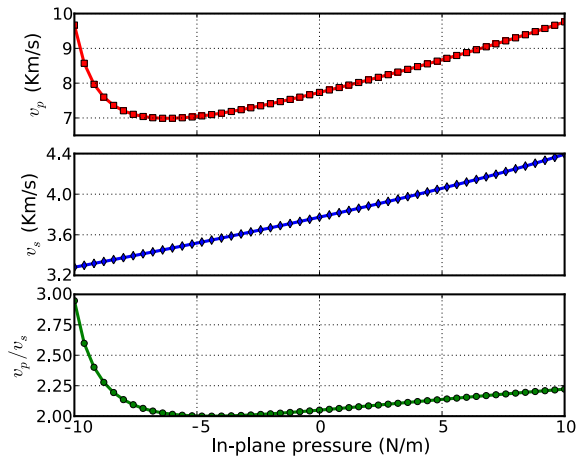

Fig. 5. *p*-Wave and *s*-wave velocities and compressional to shear wave velocity ratio v_p/v_s as a function of in-plane pressure.

The dependence of v_p and v_s on pressure (biaxial stress) is plotted in Fig. 5. There is a minima (7 km/s) of the v_p curve at an in-plane pressure of -7 GPa. However, v_s monotonically increase with an increase pressure. Thus they can be tuned by introducing the biaxial strain through the stress–strain relationship shown in Fig. 3c.

The compressional to shear wave velocity ratio (v_p/v_s) is a very useful parameter in the determination of a material's mechanical properties. It depends only on the Poisson's ratio as

$$\frac{v_p}{v_s} = \sqrt{\frac{1}{\tilde{\nu}}\left(1+\frac{\tilde{\nu}^2}{1-2\tilde{\nu}}\right)}. \tag{6}$$

The ratio of v_p/v_s monotonically increases with the increase of pressure as shown in Fig. 5.

Notice that a sound velocity gradient could be achieved by introducing stress into a *g*-GeC monolayer, which could lead to refraction of sound wavefronts in the direction of lower sound speed, causing the sound rays to follow a curved path (Everest, 2001). The radius of curvature of the sound path is inversely proportional to the gradient. Also a negative sound speed gradient could be achieved by a negative strain gradient. This tunable sound velocity gradient can be used to form a sound frequency and ranging channel, which is the functional mechanism of waveguides and surface acoustic wave (SAW) sensors (Benes et al., 1998; Weigel et al., 2002). Thus, *g*-GeC-based nano-devices of SAW sensors, filters, and waveguides may be synthesized using local strains for next generation electronics.

4. Conclusions

In summary, we studied the mechanical response of *g*-GeC under various strains using DFT based first-principles calculations. It is observed that *g*-GeC exhibits a nonlinear elastic deformation up to an ultimate strain, which is 0.18, 0.19, and 0.16 for armchair, zigzag, and biaxial directions, respectively. The deformation and failure behavior and the ultimate strength are anisotropic. It has a relatively low in-plane stiffness (143.8 N/m) and a large Poisson ratio (0.281) compared to graphene and *g*-BN.

The nonlinear elasticity of *g*-GeC was investigated. We found an accurate continuum description of the elastic properties of *g*-GeC by explicitly determining the fourteen independent components of high order (up to fifth order) elastic constants from the fitting of the stress–strain curves obtained from DFT calculations. This data is useful to develop a continuum description which is suitable for incorporation into a finite element analysis model for its applications in large scale. The second order elastic constants including in-plane stiffness are predicted to monotonically increase with pressure while Poisson's ratio monotonically decreases with increasing pressure. The sound velocity of a compressional wave has a minima at an in-plane pressure of -7 GPa while that of the shear wave monotonically increases with pressure.

Acknowledgments

The authors would like to acknowledge the generous financial support from the Defense Threat Reduction Agency (DTRA) Grant # BRBAA08-C-2–0130 and # HDTRA1–13-1–0025, U.S. Nuclear Regulatory Commission Faculty Development Program Grant # NRC-38–08-950 and U.S. Department of Energy (DOE) Nuclear Energy University Program (NEUP) Grant # DE-NE0000325.

References

Şahin, H., Cahangirov, S., Topsakal, M., Bekaroglu, E., Akturk, E., Senger, R.T., Ciraci, S., 2009. Monolayer honeycomb structures of group-IV elements and III–V binary compounds: first-principles calculations. Phys. Rev. B 80 (15), 155453.

Chigo Anota, E., Murrieta Hernandez, G., 2011. Electronic properties of germanium carbide blade of graphene type. Rev. Mex. Fis. 57 (1), 30–34.

Lu, T.-Y., Liao, X.-X., Wang, H.-Q., Zheng, J.-C., 2012. Tuning the indirect–direct band gap transition of SiC GeC and SnC monolayer in a graphene-like honeycomb structure by strain engineering: a quasiparticle GW study. J. Mater. Chem. 22 (19), 10062–10068.

Shim, I., Baba, M.S., Gingerich, K.A., 1998. Electronic structure and thermodynamic properties of the molecule GeC from all-electron ab initio calculations and Knudsen effusion mass spectrometric measurements. J. Phys. Chem. A 102 (52), 10763–10767.

Sari, L., Yamaguchi, Y., Schaefer, H.F., 2003. 3 Sigma(-) and 3 Pi states of GeC and GeSi: the problematic dissociation energy of GeC. J. Chem. Phys. 119 (16), 8266–8275.

Ueno, L.T., Marim, L.R., Dal Pino Jr., A., Ornellas, F.R., Machado, F.B.C., 2006. Transition probabilities and spectroscopic properties of the low-lying states of GeC molecule. Chem. Phys. Lett. 432 (1–3), 11–16.

Brazier, C.R., Ruiz, J.I., 2011. The first spectroscopic observation of germanium carbide. J. Mol. Spectrosc. 270 (1), 26–32.

Mahmood, A., Sansores, L., 2005. Band structure and bulk modulus calculations of germanium carbide. J. Mater. Res. 20 (5), 1101–1106.

Ganguly, G., De, S.C., Ray, S., Barua, A.K., 1991. Polycrystalline silicon-carbide films deposited by low-power radiofrequency plasma decomposition of SiF4-CF4-H2 Gas-mixtures. J. Appl. Phys. 69 (7), 3915–3923.

Lee, C., Wei, X., Kysar, J.W., Hone, J., 2008. Measurement of the elastic properties and intrinsic strength of monolayer graphene. Science 321 (5887), 385.

Liu, F., Ming, P., Li, J., 2007. Ab initio calculation of ideal strength and phonon instability of graphene under tension. Phys. Rev. B 76 (6), 064120.

Xiao, T., Xu, X., Liao, K., 2004. Characterization of nonlinear elasticity and elastic instability in single-walled carbon nanotubes. J. Appl. Phys. 95 (12), 8145.

Khare, R., Mielke, S.L., Paci, J.T., Zhang, S., Ballarini, R., Schatz, G.C., Belytschko, T., 2007. Coupled quantum mechanical molecular mechanical modeling of the fracture of defective carbon nanotubes and graphene sheets. Phys. Rev. B 75 (7), 075412.

Lu, Q., Huang, R., 2009. Nonlinear mechanics of single-atomic-layer graphene sheets. Int. J. Appl. Mech. 1 (3), 443.

Peng, Q., Ji, W., De, S., 2012a. Mechanical properties of the hexagonal boron nitride monolayer: ab initio study. Comput. Mater. Sci. 56, 11.

Peng, Q., Zamiri, A.R., Ji, W., De, S., 2012b. Elastic properties of hybrid graphene/boron nitride monolayer. Acta Mech. 223, 2591–2596.

Peng, Q., Ji, W., De, S., 2012c. Mechanical properties of graphyne monolayer: a first-principles study. Phys. Chem. Chem. Phys. 14, 13385–13391.

Hiki, Y., 1981. Higher-order elastic-constants of solids. Annu. Rev. mater. sci. 11, 51.

Cadelano, E., Palla, P.L., Giordano, S., Colombo, L., 2009. Nonlinear elasticity of monolayer graphene. Phys. Rev. Lett. 102 (23), 235502.

Wei, X., Fragneaud, B., Marianetti, C.A., Kysar, J.W., 2009. Nonlinear elastic behavior of graphene: Ab initio calculations to continuum description. Phys. Rev. B 80 (20), 205407.

Peng, Q., De, S., 2012. Tunable band gaps of mono-layer hexagonal BNC heterostructures. Phys. E 44, 1662–1666.

Peng, Q., Ji, W., De, S., 2013a. First-principles study of the effects of mechanical strains on the radiation hardness of hexagonal boron nitride monolayers. Nanoscale 5, 695–703.

Marianetti, C.A., Yevick, H.G., 2010. Failure mechanisms of graphene under tension. Phys. Rev. Lett. 105, 245502.

Kresse, G., Hafner, J., 1993. Ab initio molecular dynamics for liquid metals. Phys. Rev. B 47, 558.

Kresse, G., Hafner, J., 1994. Ab initio molecular-dynamics simulation of the liquid–metal–amorphous-semiconductor transition in germanium. Phys. Rev. B 49, 14251.

Kresse, G., Furthuller, J., 1996a. Efficient iterative schemes for ab initio total-energy calculations using a plane-wave basis set. Phys. Rev. B 54, 11169.

Kresse, G., Furthuller, J., 1996b. Efficiency of ab-initio total energy calculations for metals and semiconductors using a plane-wave basis set. Comput. Mater. Sci. 6, 15.

Hohenberg, P., Kohn, W., 1964. Inhomogeneous electron gas. Phys. Rev. 136 (3B), B864.

Kohn, W., Sham, L.J., 1965. Self-consistent equations including exchange and correlation effects. Phys. Rev. 140 (4A), A1133.

Perdew, J., Burke, K., Ernzerhof, M., 1996. Generalized gradient approximation made simple. Phys. Rev. Lett. 77, 3865.

Blöchl, P.E., 1994. Projector augmented-wave method. Phys. Rev. B 50 (24), 17953–17979.

Jones, R.O., Gunnarsson, O., 1989. The density functional formalism its applications and prospects. Rev. Mod. Phys. 61 (3), 689–746.

Peng, Q., Liang, C., Ji, W., De, S., 2012d. A first principles investigation of the mechanical properties of *g*-tln. Model. Numer. Simul. Mater. Sci. 2, 76–84.

Peng, Q., Liang, C., Ji, W., De, S., 2013b. A first principles investigation of the mechanical properties of g-zno: the graphene-like hexagonal zinc oxide monolayer. Comput. Mater. Sci. 68, 320–324.

Peng, Q., Liang, C., Ji, W., De, S., 2013c. A theoretical analysis of the effect of the hydrogenation of graphene to graphane on its mechanical properties. Phys. Chem. Chem. Phys. 15, 2003–2011.

Peng, Q., Liang, C., Ji, W., De, S., 2013d. Mechanical properties of g-gan: a first principles study. Appl. Phys. A. http://dx.doi.org/10.1007/s00339–013–7551–4.

Peng, Q., Chen, X.-J., Ji, W., De, S., 2013e. Chemically tuning mechanics of graphene by bn. Adv. Eng. Mater.. http://dx.doi.org/10.1002/adem.201300033.

Cerda, E., Mahadevan, L., 2003. Geometry and physics of wrinkling. Phys. Rev. Lett. 90, 074302.

Zhang, Y., Liu, F., 2011. Maximum asymmetry in strain induced mechanical instability of graphene: compression versus tension. Appl. Phys. Lett. 99 (24), 241908.

Tsoukleri, G., Parthenios, J., Papagelis, K., Jalil, R., Ferrari, A.C., Geim, A.K., Novoselov, K.S., Galiotis, C., 2009. Subjecting a graphene monolayer to tension and compression. Small 5 (21), 2397–2402.

Bao, W., Miao, F., Chen, Z., Zhang, H., Jang, W., Dames, C., Lau, C.N., 2009. Controlled ripple texturing of suspended graphene and ultrathin graphite membranes. Nat. Nanotech. 4 (9), 562–566.

Yoon, D., Son, Y.-W., Cheong, H., 2011. Negative thermal expansion coefficient of graphene measured by Raman spectroscopy. Nano Lett. 11 (8), 3227–3231.

Pan, W., Xiao, J., Zhu, J., Yu, C., Zhang, G., Ni, Z., Watanabe, K., Taniguchi, T., Shi, Y., Wang, X., 2012. Biaxial compressive strain engineering in graphene/boron nitride heterostructures. Sci. Rep. 2, 893.

Quhe, R., Zheng, J., Luo, G., Liu, Q., Qin, R., Zhou, J., Yu, D., Nagase, S., Mei, W.-N., Gao, Z., Lu, J., 2012. Tunable and sizable band gap of single-layer graphene sandwiched between hexagonal boron nitride. NPG Asia Mater. 4, E6.

Topsakal, M., Cahangirov, S., Ciraci, S., 2010. The response of mechanical and electronic properties of graphane to the elastic strain. Appl. Phys. Lett. 96 (9), 091912.

Everest, F., 2001. The Master Handbook of Acoustics. McGraw-Hill, New York.

Benes, E.R., Groschl, R., Seifert, F., Pohl, A., 1998. Comparison between BAW and SAW sensor principles. IEEE Trans. Ultrason. Ferroelectr. Freq. Control 45 (5), 1314–1330.

Weigel, R., Morgan, D.P., Owens, J.M., Ballato, A., Lakin, K.M., Hashimoto, K., Ruppel, C.C.W., 2002. Microwave acoustic materials devices and applications. IEEE Trans. Microwave Theory Tech. 50 (3), 738–749.